FORMATION DESIGN ANALYSIS FOR A MINIATURIZED DISTRIBUTED OCCULTER/TELESCOPE IN EARTH ORBIT

Adam W. Koenig(1), **Simone D'Amico**(2), **Bruce Macintosh**(3), **and Charles J. Titus**(4)
(1)(2)*Stanford University, Department of Aeronautics & Astronautics, Space Rendezvous Laboratory, Durand Building, 496 Lomita Mall Stanford, CA 94305, awkoenig@stanford.edu*
(3)(4)*Stanford University, Department of Physics, 382 Via Pueblo Mall, Stanford, CA 94305, bmacintosh@stanford.edu*

Abstract:

This paper extends a recently proposed formation design methodology for a miniaturized distributed occulter/telescope (mDOT). In contrast to large-scale missions such as the New Worlds Observer or Exo-S (NASA), mDOT makes use of micro- and nano-satellites inertially aligned in earth orbit to reduce mission costs by orders of magnitude. Due to the small telescope aperture, this concept requires greater instrument integration time (or observation duration) in an environment with larger differential accelerations. Consequently, a delta-v optimal design of the absolute and relative orbits represents a mission enabler. The proposed formation design strategy stems from the fundamental idea that the delta-v cost of observations can be minimized by allowing the formation to freely drift along the line-of-sight. This paper makes two key contributions to the state of the art. First, it is demonstrated through high-fidelity numerical simulations that third body, solar radiation pressure, and atmospheric drag forces have negligible impact on the delta-v cost of mission operations. Second, the cost associated with a reference mission is characterized as a function of the location of the science target. This characterization is performed with and without a constraint that observations are performed with the occulter spacecraft in earth's umbra. This constraint ensures that light reflected by the occulter does not overwhelm the signal from the science target.

Keywords: *formation flying design, orbit design, maneuver planning, exoplanet imaging, starshades*

1. Introduction

The astrophysics community has shown increasing interest in detection and characterization of exoplanets in recent years. While initial discoveries were made with Doppler or barycenter offset methods, more recent detection efforts rely on precise transit photometry measurements. Most notably, NASA's Kepler mission is now responsible for more than one thousand confirmed exoplanet discoveries [1]. The indirect methods used for most discoveries to date allow scientists to determine the mass, size, and temperature of a planet, but provide little information about its chemical composition. The necessary data for this level of characterization can only be acquired via direct imaging. Spectroscopy data collected from direct images would allow scientists to identify key biosignature gases such as oxygen, water, and carbon dioxide. The capabilities of guidance, navigation, and control (GN&C) systems deployed on recent formation flying missions [2, 3, 4] suggest that it may be possible to directly image exoplanets using a distributed occulter/telescope. Indeed, studies of the distributed occulter/telescope have resulted in several mission concepts including Exo-S (NASA) [5] and the New Worlds Observer (NASA) [6], which aim to image multiple earth-like planets in the visible spectrum. However, the estimated cost of these missions is in the billions of dollars.

To minimize the risk associated with such a costly mission, the authors recently proposed a miniaturized distributed occulter/telescope (mDOT) mission to image exozodiacal dust disks using two micro- or nano-satellites in earth orbit [7, 8]. This technology demonstrator would serve to 1) demonstrate the validity of the distributed occulter/telescope concept, 2) facilitate development of key enabling technologies for a full-scale system, and 3) directly image a small set of targets of scientific interest. The authors forsee an occulter of diameter no larger than 2 m separated from a 10 cm diameter telescope by several hundred kilometers. The occulter will be designed to suppress some specified bandwidth in the ultraviolet spectrum (150-400 nm). A novel feature of the proposed concept is that the spacecraft are allowed to drift along the line-of-sight during observations. Thus, the GN&C system need only counteract differential accelerations perpendicular to the line-of-sight during observations.

It is evident that the delta-v cost associated with mission operations should be minimized in order to maximize the science return of a small-scale mission. To that end, this paper presents two findings on the delta-v cost of mDOT missions in earth orbit. First, after a concise derivation of the delta-v optimal formation design recently proposed by the authors [8], it is demonstrated through high-fidelity numerical simulations that third body, solar radiation pressure, and atmospheric drag forces have negligible impact on the delta-v cost of nominal operations. Second, the delta-v cost of a reference mission profile is characterized as a function of the location of the science target. This characterization is performed with and without a constraint that observations are performed with the occulter spacecraft in earth's umbra. This constraint ensures that reflected light from the occulter does not overwhelm the signal from the science target.

2. Science Target Modeling

Extrasolar planets are not the only high-contrast imaging targets of interest around nearby stars. In addition to its planetary system, our sun is orbited by asteroids and comets. Collisions and erosion of these bodies produces the zodiacal dust. This both scatters sunlight and re-emits absorbed sunlight in the thermal infrared. The integrated light from zodiacal dust is actually a hundred times brighter than Jupiter - in our solar system, the flux due to dust is $F_{disk}/F_{star} = 10^{-7}$ of the luminosity of the sun. Similar disks have been detected around many nearby stars through thermal emission, which is observed as excess infrared flux compared to the predicted stellar spectrum (the Vega phenomenon). These detections show that for many stars the total mass of dust is much higher than in our solar system, with F_{disk}/F_{star} as high as 10^{-3}. In most cases, the dust disk has been detected only through thermal emission at long wavelengths. Visible or near-infrared scattered light has been seen in some favorable cases (e.g. Beta Pictoris) with coronagraphy, but detecting the scattered light from these disks would be scientifically extremely interesting. Comparison of ultraviolet to visible and infrared brightness would help constrain the size of the scattering particles, and polarization properties could even provide information about their shape [9]. Detecting these disks is therefore both practical and scientifically compelling. Fig. 1 shows exposure times needed to detect a disk with the same geometry as that orbiting Beta Pictoris as a function of F_{disk}/F_{star} for a fiducial telescope model specified in Tab. 1 and an assumed occulter contrast of 10^{-7}. Since in many cases it is possible to identify systems with $F_{disk}/F_{star} > 10^{-5}$ via infrared techniques [10], promising science targets can be identified in advance of a mission.

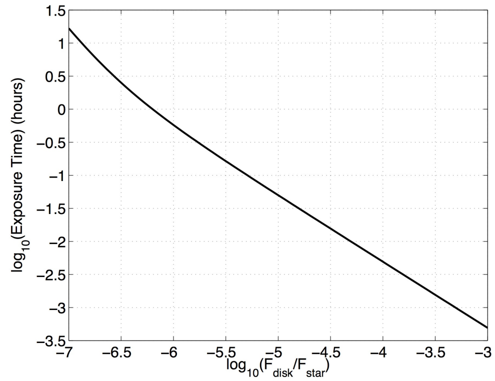

Figure 1. Necessary exposure time for detection of reference exozodiacal dust disk vs fractional brightness for fiducial telescope model

Table 1. Fiducial telescope model

Diameter	10 cm
Bandpass	200-300 nm
Throughput of camera	79%
QE of detector	80%
Read noise	3 e^-/pixel
Dark current	0.0016 e^-/(pixel sec)

3. Proposed Concept Description

It is evident from the discussion in the previous section that scientifically interesting targets may require several hours of integration time to detect. Considering the limits of small satellite GN&C systems, conducting such a long observation in one continuous pass in earth orbit is highly impractical. Thus, the envisioned mission operations strategy includes two phases: 1) a science phase during which a low-thrust, continuous control system is used to maintain decimeter-level relative position control while the telescope instrument images the target from within the shadow of the occulter, and 2) a reconfiguration phase during which the formation is reconfigured by a sequence of impulsive maneuvers to ensure proper alignment at the start of the next science phase. The proposed operations concept is illustrated in Fig. 2. This operations strategy is inspired by the European Space Agency's PROBA-3 solar coronagraph concept [11], but is subject to several distinct challenges. First, the baseline separation of the mDOT concept is several hundred kilometers, orders of magnitude larger than the PROBA-3 baseline. Additionally, the mDOT concept is subject to the onboard resource limitations of micro-/nano-satellites.

It has been demonstrated that it is possible to design a small occulter capable of achieving sufficient contrast to image exozodiacal dust disks over a small range of separation distances ($\pm 1\%$ of the

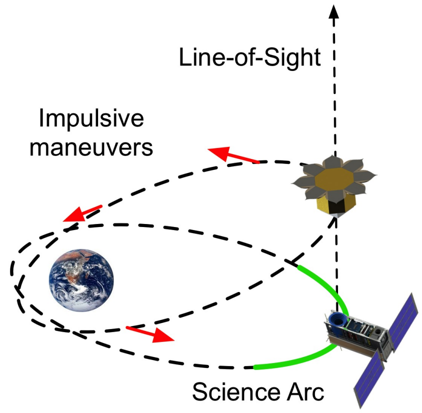

Figure 2. Illustration of telescope and occulter orbits (not to scale) noting forced motion control during the science phase (green) and impulsive control during the reconfiguration phase (red)

baseline [7]). The proposed concept exploits this separation insensitivity by allowing the spacecraft to freely drift along the line-of-sight during observations. Thus, the GN&C system need only counteract differential accelerations perpendicular to the line-of-sight.

4. Science Phase Cost Modeling

The following is a concise derivation of the delta-v optimal formation design based on considerations of science phase maneuvers. First, an analytical formulation of the delta-v cost of a family of pareto-optimal forced motion control maneuvers is presented. This formulation is used to select the initial argument of perigee and right ascension of the ascending node (RAAN) that minimizes the deviation of the formation from the optimal configuration over the expected mission lifetime. For more detailed discussions of this formation design, the reader is referred to Koenig et al. [8].

4.1. Instantaneous Cost Modeling

Figure 3 illustrates the mDOT formation in earth orbit with relevant design variables. In this model the inertial position and velocity vectors of the telescope are expressed by $\mathbf{r}$ and $\mathbf{v}$, respectively. A rotating orbit frame (RTN) centered at the telescope is defined by the radial (R, along $\mathbf{r}$), cross-track (N, along orbit normal), and along-track (T, completes right-handed triad) directions. The relative position vector of the occulter in the RTN frame, $\boldsymbol{\rho}$, can be decomposed into component displacements x, y, and z in the R, T, and N directions, respectively. In this model, the inertial differential acceleration between the occulter and telescope spacecraft, $\delta\mathbf{g}$, due to spherical earth gravity is given in the RTN frame by

$$\delta\mathbf{g} = \mu \begin{bmatrix} \frac{1}{r^2} - \frac{r+x}{\left((r+x)^2+y^2+z^2\right)^{3/2}} \\ -\frac{y}{\left((r+x)^2+y^2+z^2\right)^{3/2}} \\ -\frac{z}{\left((r+x)^2+y^2+z^2\right)^{3/2}} \end{bmatrix} \tag{1}$$

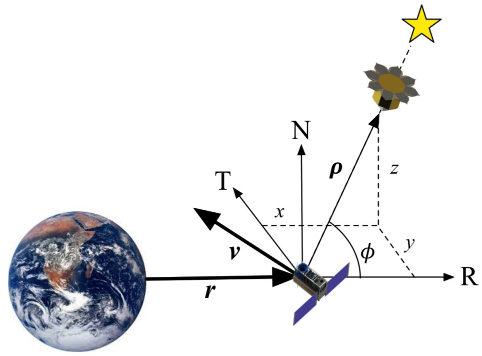

Figure 3. Illustration of mDOT formation in earth orbit (not to scale) with relevant design variables

where μ denotes earth's gravitational parameter. The component of this acceleration orthogonal to the line-of-sight, $\delta g_\perp$, is computed by taking the norm of the difference between $\boldsymbol{\delta g}$ and its projection onto $\boldsymbol{\rho}$, as given by

$$\delta g_\perp = ||\boldsymbol{\delta g} - \frac{\boldsymbol{\delta g}\cdot\boldsymbol{\rho}}{||\boldsymbol{\rho}||}\boldsymbol{\rho}|| = \mu\sqrt{\frac{y^2+z^2}{x^2+y^2+z^2}}\left[\frac{r}{((r+x)^2+y^2+z^2)^{3/2}} - \frac{1}{r^2}\right] \tag{2}$$

Using the identities $\rho = \sqrt{x^2+y^2+x^2}$ and $\phi = \arccos(x/\rho)$, which can be derived from Fig. 3, Eq. 2 can be simplified to

$$\delta g_\perp = \mu\sin\phi\left[\frac{r}{(r^2+2r\rho\cos\phi+\rho^2)^{3/2}} - \frac{1}{r^2}\right] \tag{3}$$

Inspection of Eq. 3 reveals that there exist two non-trivial conditions that reduce $\delta g_\perp$ to zero. The first condition is given by $\phi = 0$, which corresponds to a formation aligned with the radial direction. However, because the relative velocity between the spacecraft during an observation must be small, it is evident that spacecraft aligned in the radial direction will have different mechanical energies. It follows that these formations are characterized by a large difference in semi-major axis. In order to perform periodic observations, it is necessary to remove and re-establish this baseline between science phases. The authors have found from simulations that the delta-v cost of these maneuvers is impractically large.

The second and more interesting condition that reduces $\delta g_\perp$ to zero occurs when $\phi = \arccos(-\rho/2r)$, which corresponds to a formation characterized by equal radii of the telescope and occulter orbits. Equivalently, this second condition corresponds to a formation aligned in the along-track/cross-track, TN, plane defined through curvilinear coordinates [12]. The delta-v cost of the science phase is minimized by ensuring that the formation remains near this configuration for the duration of a finite maneuver.

4.2. Separation Drift Modeling

Because the proposed operations strategy only counteracts differential acceleration perpendicular to the line-of-sight, the spacecraft will tend to drift over the course of a science phase. Indeed, the resulting change in separation can be as large as several kilometers for long observations. With this in mind, the following analysis will demonstrate that the maximum allowable observation duration depends only on separation drift allowed by the optical system and the orbit radius when the observation is performed. Let $\bar{\rho}$ denote the baseline inter-spacecraft separation specified by the optical system. For two spacecraft with equal orbit radii, the differential acceleration along the line-of-sight, $\ddot{\rho}$, is computed from simple trigonometry according to

$$\ddot{\rho} = -2\frac{\mu}{r^2}\sin\left(\frac{\bar{\rho}}{2r}\right) \approx -\frac{\mu\bar{\rho}}{r^3} \tag{4}$$

If it is assumed that $\ddot{\rho}$ is constant over the duration of an observation, the time history of the inter-spacecraft separation can be modeled as a parabola according to

$$\rho(t) = \rho(t_0) + \dot{\rho}(t_0)(t-t_0) + 0.5\ddot{\rho}(t-t_0)^2 \tag{5}$$

where $\rho(t)$ denotes the magnitude of the relative position vector at time t, $\dot{\rho}(t)$ denotes to the derivative with respect to time of $\rho(t)$, and t_0 denotes the start time of the science phase maneuver. It is desirable to minimize the maximum deviation of $\rho(t)$ from $\bar{\rho}$ over the course of an observation. If the maneuver duration is given by Δt, then the initial separation, $\rho(t_0)$, and drift velocity, $\dot{\rho}(t_0)$, that minimize the deviation from the baseline separation are given by

$$\rho(t_0) = \bar{\rho}\left(1 - \frac{\mu\Delta t^2}{16r^3}\right) \qquad \dot{\rho}(t_0) = \frac{\mu\bar{\rho}\Delta t}{2r^3} \tag{6}$$

According to this model the maximum separation deviation, $\Delta\rho$, normalized by the baseline separation is given by

$$\frac{\Delta\rho}{\bar{\rho}} = \frac{\mu\Delta t^2}{16r^3} \tag{7}$$

Finally, if we assume the maximum allowable ratio $\Delta\rho/\bar{\rho}$ is fixed by the optical system, the maximum allowable observation time, Δt_{max}, is given by

$$\Delta t_{max} = \sqrt{\frac{16r^3}{\mu}\frac{\Delta\rho}{\bar{\rho}}} \tag{8}$$

It is clear that Δt_{max} depends only on the orbit radius and the drift tolerance of the optical system. Additionally, it can be seen that allowing ρ to drift by only 1% is sufficient to ensure that a 1-hour long observation will not violate optical requirements as long as the orbit radius is at least 30000 km.

4.3. Finite Maneuver Cost Modeling

At this point, it has been established that there exist configurations such that the differential acceleration perpendicular to the line-of-sight is identically zero. It is now possible to compute the delta-v cost associated with a finite maneuver, $\Delta v_{science}$, as given by

$$\Delta v_{science} = \int_{t_0}^{t_0+\Delta t} |g_{\perp}(t)|dt \tag{9}$$

If the duration of the maneuver is short compared to the orbit period, it is reasonable to approximate the evolution of $\delta g_\perp$ as a linear function given by

$$\delta g_\perp(t) = \frac{D\delta g_\perp}{Dt}\left(t - t_0 - \frac{\Delta t}{2}\right) + \delta g_{\perp 0} \qquad \frac{D\delta g_\perp}{Dt} = \frac{\delta \delta g_\perp}{\delta r}\frac{dr}{dt} + \frac{\delta \delta g_\perp}{\delta \rho}\frac{d\rho}{dt} + \frac{\delta \delta g_\perp}{\delta \phi}\frac{d\phi}{dt} \tag{10}$$

where $\delta g_{\perp 0}$ and $D\delta g_\perp/Dt$ denote the differential acceleration perpendicular to the line-of-sight and its substantial derivative, respectively, evaluated at $t = t_0 + \Delta t/2$. The total delta-v cost of the maneuver is minimized by selecting the start time of the maneuver such that $\delta g_{\perp 0} = 0$. The expression of the substantial derivative can be greatly simplified with a few assumptions. First, it is known from classical Keplerian mechanics [12] that the time rate of change of the orbit radius at the apogee of an eccentric orbit (corresponding to the maximum orbit radius) or anywhere in a circular orbit is zero. Thus, the r-dependent terms of the substantial derivative can be neglected. Additionally, it is known that ρ must be kept nearly constant to satisfy the requirements of the optical system. Thus, the ρ-dependent terms can also be neglected. The simplified substantial derivative of the instantaneous cost is given by

$$\frac{D\delta g_\perp}{Dt} = \frac{\delta \delta g_\perp}{\delta \phi}\frac{d\phi}{dt} \tag{11}$$

which depends only on the behavior of ϕ. The time evolution of ϕ is a function of the pointing vector to an inertial target expressed in the RTN frame. This pointing vector is a function of the classical Keplerian orbit elements including true anomaly, ν, argument of perigee, ω, inclination, i, and RAAN, Ω. The transformation between the earth-centered inertial (ECI) and RTN frames is given by the following sequence of elementary rotation matrices

$$\hat{\boldsymbol{\rho}}^{RTN} = \mathbf{R}_3(\nu)\mathbf{R}_3(\omega)\mathbf{R}_1(i)\mathbf{R}_3(\Omega)\hat{\boldsymbol{\rho}}^{ECI} \tag{12}$$

where $\mathbf{R}_i$ denotes a rotation about the i^{th} axis. With the exception of true anomaly, the orbit elements evolve very slowly and only due to forces other than spherical earth gravity. For simplicity, the slowly varying terms are grouped in a vector defined by

$$\hat{\boldsymbol{\rho}}^{PQR} = \mathbf{R}_3(\omega)\mathbf{R}_1(i)\mathbf{R}_3(\Omega)\hat{\rho}^{ECI} = \begin{bmatrix} \sqrt{1-\gamma^2}\cos\nu^* \\ \sqrt{1-\gamma^2}\sin\nu^* \\ \gamma \end{bmatrix} \tag{13}$$

where $\hat{\boldsymbol{\rho}}^{PQR}$ represents the pointing vector to the target expressed in perifocal coordinates. In this relation, ν^* denotes the phase angle of the projection of the pointing vector onto the orbit plane and γ denotes the cross-track component of the pointing vector. This parameterization of the pointing vector is selected to simplify the following formulations. Substituting Eq. 13 in Eq. 12 yields

$$\hat{\boldsymbol{\rho}}^{RTN} = \rho\,\mathbf{R}_3(\nu)\begin{bmatrix} \sqrt{1-\gamma^2}\cos\nu^* \\ \sqrt{1-\gamma^2}\sin\nu^* \\ \gamma \end{bmatrix} = \rho\begin{bmatrix} \sqrt{1-\gamma^2}\cos(\nu^*-\nu) \\ \sqrt{1-\gamma^2}\sin(\nu^*-\nu) \\ \gamma \end{bmatrix} \tag{14}$$

which parameterizes the evolution of the pointing vector in the RTN frame as a function of ν, ν^*, and γ. From Eq. 14 it is clear that the motion of the pointing vector to an inertial target is characterized by a circle in the radial/along-track plane with a constant offset in the cross-track direction.

Now that the evolution of the pointing vector to the target has been characterized, the substantial derivative of $\delta g_\perp$ can be evaluated. Because ϕ is the angle between the pointing vector to the target and the radial direction, it can be expressed as a function of ν, ν^*, and γ as given by

$$\cos\phi = \sqrt{1-\gamma^2}\cos(\nu^* - \nu) \tag{15}$$

Because ϕ is expressed as a function of ν, the substantial derivative given in Eq. 11 can be expanded by applying the chain rule, which yields

$$\frac{D\delta g_\perp}{Dt} = \frac{\delta \delta g_\perp}{\delta \phi}\frac{d\phi}{d\nu}\frac{d\nu}{dt} \tag{16}$$

From Eq. 3, the partial derivative of $\delta g_\perp$ with respect to ϕ evaluated at $\cos\phi = -\rho/(2r)$ is given by

$$\frac{\delta \delta g_\perp}{d\phi} = \frac{3\mu\rho}{r^3}\left(1-\frac{\rho^2}{4r^2}\right) \tag{17}$$

From Eq. 15, the derivative of ϕ with respect to ν evaluated at $\cos\phi = -\rho/(2r)$ is given by

$$\frac{d\phi}{d\nu} = \frac{\sin(\nu^*-\nu)}{\sqrt{(1-\gamma^2)\sin^2(\nu^*-\nu)+\gamma^2}} = \frac{\sqrt{1-\gamma^2-\frac{\rho^2}{4r^2}}}{\sqrt{1-\frac{\rho^2}{4r^2}}} \tag{18}$$

and the time rate of change of ν is given from classical Keplerian mechanics [12] by

$$\frac{d\nu}{dt} = \frac{\sqrt{\mu a(1-e^2)}}{r^2} \tag{19}$$

Combining Eqs. 16-19 yields

$$\frac{Dg_\perp}{Dt} = \frac{3\mu\rho}{r^5}\sqrt{\mu a(1-e^2)\left(1-\frac{\rho^2}{4r^2}\right)\left(1-\gamma^2-\frac{\rho^2}{4r^2}\right)} \tag{20}$$

Finally, substituting Eqs. 10 and 20 into Eq. 9 yields

$$\Delta v_{science} = \int_{t_0}^{t_0+\Delta t}(t-t_0-\frac{\Delta t}{2})\frac{3\mu\rho}{r^5}\sqrt{\mu a(1-e^2)\left(1-\frac{\rho^2}{4r^2}\right)\left(1-\gamma^2-\frac{\rho^2}{4r^2}\right)}dt \tag{21}$$

which can be evaluated directly. The resulting delta-v cost is given by

$$\Delta v_{science} = \frac{3\mu\rho\Delta t^2}{4r^5}\sqrt{\mu a(1-e^2)\left(1-\frac{\rho^2}{4r^2}\right)\left(1-\gamma^2-\frac{\rho^2}{4r^2}\right)} \tag{22}$$

Equation 22 presents an analytical expression for the delta-v cost associated with a finite forced motion control maneuver to achieve constant inertial pointing. This expression was developed by integrating an analytical expression of the differential acceleration perpendicular to the line-of-sight due to spherical earth gravity. There are three key assumptions used in this derivation: 1) The maneuver is centered about a configuration where the instantaneous cost as defined by Eq. 3 is zero, 2) the orbit radius is constant during the maneuver, and 3) the inter-spacecraft separation is constant during the maneuver. There are a number of important conclusions that can be drawn from Eq. 22. First, the delta-v cost depends very strongly on the orbit radius. Thus, the orbit semi-major axis should be maximized in order to minimize cost. Second, increasing the eccentricity of the orbit reduces the delta-v cost of a science phase maneuver performed at the apogee. Third, the cost depends on the parameter γ, which is an analog of the cross-track component of the relative position vector. Specifically, configurations that satisfy $\gamma^2 = 1 - \rho^2/(4r^2)$ have a delta-v cost of zero to first order. Maximizing $|\gamma|$ requires that the pointing vector to the target is perpendicular to the orbit plane. There are two sets of i and Ω that satisfy $|\gamma| = 1$ for an arbitrary science target. These correspond to cases where the orbit angular momentum vector is either parallel or anti-parallel to the pointing vector to the target. It should be noted that Eq. 22 only applies to orbits that satisfy $|\gamma| \leq \sqrt{1 - \rho^2/(4r^2)}$. However, orbits that violate this constraint will remain very close to the instantaneous zero-cost configuration.

Fig. 4 (left) illustrates the behavior of $\Delta v_{science}$ for 1-hour long observations for an mDOT formation in a circular orbit with a 500 km baseline separation for a range of orbit semi-major axis and γ values. It can be seen that unless the formation has a very high value of $|\gamma|$, it is essential that the orbit be as large as possible. To validate the assumptions used in the derivation of Eq. 22, Fig. 4 (right) compares the delta-v cost from the analytical formula with the delta-v cost computed from high-fidelity numerical simulations with the GRACE Gravity model GGM01S of degree and order 120 [13] for a formation with a 40000 km orbit radius for various values of γ. It can be seen that the analytical model agrees with simulation results to within 1%.

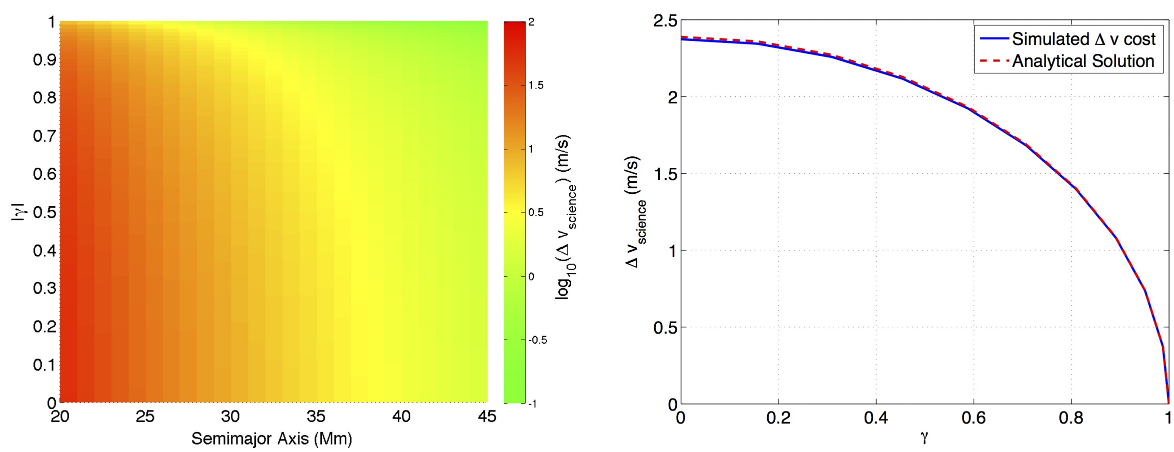

Figure 4. Optimal science phase delta-v cost for 1-hour observations in a circular orbit vs a and γ (left) and comparison with simulation (right)

4.4. Secular Drift Effects

The preceding analysis was performed under the assumption that the orbit orientation is constant. In order to fully minimize the delta-v cost of a multi-orbit mission, it is necessary to select the initial orbit such that the deviation from the optimal formation due to J_2 effects is minimized. Specifically, the initial value of the argument of perigee and RAAN should be selected with two considerations in mind: 1) the maximum difference between the angular momentum vector of the orbit and the pointing vector to the target over the expected mission lifetime should be minimized, and 2) the pointing vector to the target at the science phase location (e.g. the apogee of an eccentric orbit) should closely follow the TN-plane. Before proceeding, it is first insightful to consider the conventional definition of the pointing vector to a star. The position of a star is frequently described by two angles: the right ascension, α, and declination, δ. From these angles, the pointing vector to the science target in the ECI frame, $\hat{\boldsymbol{\rho}}_{target}^{ECI}$, is given by

$$\hat{\boldsymbol{\rho}}_{target}^{ECI} = \begin{bmatrix} \cos\alpha\cos\delta \\ \sin\alpha\cos\delta \\ \sin\delta \end{bmatrix} \tag{23}$$

Recall from Eq. 12 that the pointing vectors expressed in the RTN and ECI frames are related by a sequence of elementary rotations. However, the angular momentum vector of the orbit depends only on i and Ω. Consider an orbit with an argument of perigee and true anomaly of zero. Under this assumption, the pointing vector in the RTN frame is given by

$$\hat{\boldsymbol{\rho}}_{target}^{RTN} = \mathbf{R}_1(i)\mathbf{R}_3(\Omega)\hat{\boldsymbol{\rho}}_{target}^{ECI} = \begin{bmatrix} \cos\Omega & \sin\Omega & 0 \\ -\cos i\sin\Omega & \cos i\cos\Omega & \sin i \\ \sin i\sin\Omega & -\sin i\cos\Omega & \cos i \end{bmatrix} \begin{bmatrix} \cos\alpha\cos\delta \\ \sin\alpha\cos\delta \\ \sin\delta \end{bmatrix} \tag{24}$$

Combining the terms in this equation yields

$$\hat{\boldsymbol{\rho}}_{target}^{RTN} = \begin{bmatrix} \cos\delta\cos(\alpha-\Omega) \\ \cos i\cos\delta\sin(\alpha-\Omega)+\sin i\sin\delta \\ -\sin i\cos\delta\sin(\alpha-\Omega)+\cos i\sin\delta \end{bmatrix} \tag{25}$$

The necessary and sufficient condition to align the pointing vector with the angular momentum vector is that the first two terms of this expression are zero. There are two solutions that meet this requirement, which are given by

$$(\Omega_1, i_1) = (\alpha+\pi/2, -\delta+\pi/2) \qquad (\Omega_2, i_2) = (\alpha-\pi/2, \delta+\pi/2) \tag{26}$$

These solutions correspond to angular momentum vectors aligned parallel and anti-parallel, respectively, to the pointing vector to the target. The change in the pointing vector to the target in the RTN frame, $\Delta\hat{\boldsymbol{\rho}}_{target}^{RTN}$, due to a small change in the RAAN, $\Delta\Omega$, is given by

$$\Delta\hat{\boldsymbol{\rho}}_{target}^{RTN} = \Delta\Omega \begin{bmatrix} \cos\delta\sin(\alpha-\Omega) \\ -\cos i\cos\delta\cos(\alpha-\Omega) \\ \sin i\cos\delta\cos(\alpha-\Omega) \end{bmatrix} \tag{27}$$

Substitution of the first solution from Eq. 26 yields

$$\Delta\hat{\boldsymbol{\rho}}_{target}^{RTN} = \begin{bmatrix} -\cos\delta\Delta\Omega \\ 0 \\ 0 \end{bmatrix} \tag{28}$$

We have thus far assumed that the argument of perigee and true anomaly are zero. It is now convenient to generalize this expression to orbits with arbitrary argument of perigee. The perturbation of the pointing vector in the RTN frame at the apogee of such an orbit is given by

$$\Delta\hat{\boldsymbol{\rho}}_{target}^{RTN} = \mathbf{R}_3(\omega+\pi)\begin{bmatrix}-\cos\delta\Delta\Omega\\ 0\\ 0\end{bmatrix} = \cos\delta\Delta\Omega\begin{bmatrix}\cos\omega\\ -\sin\omega\\ 0\end{bmatrix} \tag{29}$$

Finally, the resulting pointing vector to the target at the apogee is given by

$$\hat{\boldsymbol{\rho}}_{target}^{RTN} = \begin{bmatrix}\cos\omega\cos\delta\Delta\Omega\\ -\sin\omega\cos\delta\Delta\Omega\\ 1\end{bmatrix} \tag{30}$$

Equation 30 describes the pointing vector to the target in the RTN frame at the apogee of an orbit where the angular momentum is misaligned with the target due to a RAAN perturbation. This misalignment introduces a component of the pointing vector in the RT-plane and the direction of this component depends on the argument of perigee. In order to ensure that the pointing vector evolves in the TN-plane, the optimal values of the argument of perigee are 90° and 270°.

The above considerations define the ideal values of Ω, i, and ω for a specific science target. Because J_2 causes a secular drift in Ω and ω, the delta-v cost associated with J_2 effects is minimized by simply centering these parameters about their desired values over the expected mission lifetime. The secular drift per orbit in radians of the RAAN and argument of perigee, denoted $\Delta\Omega$ and $\Delta\omega$, are given from the Gauss variational equations [14] by

$$\Delta\Omega = -3\pi J_2\left(\frac{R_E}{a(1-e^2)}\right)^2\cos i \qquad \Delta\omega = 1.5\pi J_2\left(\frac{R_E}{a(1-e^2)}\right)^2(5\cos^2 i-1) \tag{31}$$

Now, let Ω^* and ω^* denote the desired values of the RAAN and argument of perigee. If the expected mission duration is N orbits, the ideal choices for the initial values of the RAAN and argument of perigee, denoted Ω_0 and ω_0, are given by

$$\Omega_0 = \Omega^* - 0.5N\Delta\Omega \qquad \omega_0 = \omega^* - 0.5N\Delta\omega \tag{32}$$

It is evident from the preceding analysis that the precession of the orbit due to J_2 depends on the inclination of the orbit, which is specified by the location of the science target of interest. Noting the dependence of the orbit alignment on Ω, one could conceive an alternative operations strategy that uses a sequence of maneuvers to counteract the RAAN drift, ensuring that the absolute orbit of the formation is always optimal. The cost associated with counteracting the RAAN drift over a single orbit using a maneuver performed at the apogee is given from the Gauss variational equations [14] by

$$\Delta v = 1.5\pi J_2\sqrt{\frac{\mu(1-e)}{a(1+e)}}\left(\frac{R_E}{a(1-e^2)}\right)^2\sin(2i) \tag{33}$$

However, comparison with the total delta-v cost of missions using the previously described formation design strategy reveals that this cost is impractically large.

5. Earth Umbra Constraint Model

The previous analysis defines the optimal formation for a specified science target of interest. However, a realized mission may be subject to operational constraints that render deployment of the formation in the optimal configuration infeasible. Recall that exozodiacal dust disks are several orders of magnitude more faint than their parent stars. In order to successfully image these disks, it is imperative that the light reflected from the occulter to the telescope be less intense than the light from the science target. Thus, it is desirable to minimize the exposure of the occulter to bright light (e.g. sunlight and earth albedo) during the science phase. One method of accomplishing this is to ensure that the science phase occurs when the occulter spacecraft is in earth's umbra. Implementation of such a strategy constrains both the orbit orientation (Ω, i, and ω), and the time of year of the mission. The authors previously demonstrated that the cost associated with a reference mission is very sensitive to inclination and RAAN perturbations, but exhibits low sensitivity to argument of perigee perturbations [8]. It will now be demonstrated that it is possible to select an orbit with an apogee in the center of earth's umbra such that the angular momentum vector is aligned with the pointing vector to an arbitrary science target, provided that the argument of perigee and time of year of the mission can be freely selected. Deploying the formation in the resulting orbit minimizes the cost increase associated with the umbra constraint.

Neglecting small perturbations due to precession and nutation of earth's rotation axis, the pointing vector to the sun in the ECI frame, $\hat{\boldsymbol{\rho}}_{sun}^{ECI}$, traverses a circle over the course of a year. This pointing vector is given by

$$\hat{\boldsymbol{\rho}}_{sun}^{ECI} = \begin{bmatrix} -\cos\left(2\pi t_{mission}\right) \\ -\cos\varepsilon\sin\left(2\pi t_{mission}\right) \\ -\sin\varepsilon\sin\left(2\pi t_{mission}\right) \end{bmatrix} \tag{34}$$

where $t_{mission}$ is the amount of time since the vernal equinox measured in years and ε is the angle between earth's rotation axis and the ecliptic pole ($\sim$23.5$^{\text{o}}$). The pointing vector to the sun is always perpendicular to the pointing vector to the ecliptic pole, $\hat{\boldsymbol{\rho}}_{ecliptic}^{ECI}$, which is given by

$$\hat{\boldsymbol{\rho}}_{ecliptic}^{ECI} = \begin{bmatrix} 0 \\ -\sin\varepsilon \\ \cos\varepsilon \end{bmatrix} \tag{35}$$

Placing the orbit apogee in the center of earth's umbra is equivalent to aligning the eccentricity vector of the orbit with the pointing vector to the sun. Because the eccentricity vector must also be perpendicular to the pointing vector to the target to properly align the angular momentum vector, the ideal direction of the eccentricity vector can be computed by taking the cross product of the pointing vectors to the ecliptic pole and the science target as given by

$$\hat{\boldsymbol{\rho}}_{perigee}^{ECI} = \pm\frac{\hat{\boldsymbol{\rho}}_{ecliptic}^{ECI}\times\hat{\boldsymbol{\rho}}_{target}^{ECI}}{||\hat{\boldsymbol{\rho}}_{ecliptic}^{ECI}\times\hat{\boldsymbol{\rho}}_{target}^{ECI}||} \tag{36}$$

Now that the eccentricity vector has been computed, it is necessary to compute the corresponding argument of perigee. This can be expressed as a function of the location of the science target as given by

$$\begin{bmatrix}1\\0\\0\end{bmatrix} = \mathbf{R}_3(\omega^*)\mathbf{R}_1(i)\mathbf{R}_3(\Omega)\hat{\rho}^{ECI}_{perigee} = \mathbf{R}_3(\omega^*)\mathbf{R}_1(-\delta+90^o)\mathbf{R}_3(\alpha+90^o)\hat{\boldsymbol{\rho}}^{ECI}_{perigee} \tag{37}$$

Multiplication by $\mathbf{R}_3(-\omega^*)$ yields

$$\begin{bmatrix}\cos\omega^*\\ \sin\omega^*\\ 0\end{bmatrix} = \begin{bmatrix}-\sin\alpha & \cos\alpha & 0\\ -\sin\delta\cos\alpha & -\sin\delta\sin\alpha & \cos\delta\\ \cos\delta\cos\alpha & \cos\delta\sin\alpha & \sin\delta\end{bmatrix}\hat{\boldsymbol{\rho}}^{ECI}_{perigee} \tag{38}$$

Finally, if p_x, p_y, and p_z denote the x, y, and z components of $\hat{\boldsymbol{\rho}}^{ECI}_{perigee}$, respectively, then the argument of perigee that centers the apogee in earth's umbra and the corresponding mission time are given in closed form by

$$\omega^* = \arctan\left(\frac{-p_x\sin\delta\cos\alpha - p_y\sin\delta\sin\alpha + p_z\cos\delta}{-p_x\sin\alpha + p_y\cos\alpha}\right) \qquad t_{mission} = \frac{1}{2\pi}\arctan\left(\frac{p_y}{p_x\cos\varepsilon}\right) \tag{39}$$

For a multi-orbit mission, the initial value of the argument of perigee should be selected to center the orbit about ω^* over the expected mission lifetime. Additionally, it is evident that there are two suitable mission times and corresponding values of ω^* that properly orient the orbit with respect to earth's umbra. These points are exactly six months apart and the corresponding arguments of perigee are separated by 180°. Figure 5 illustrates how ω^* varies with the declination and right ascension of the science target. For clarity, only values between 0° and 180° are shown. It can be seen that there exist a small family of targets that allow for $\omega^* \approx 90°$ (green), but for most targets the required argument of perigee is close to 23° (blue) or 157° (red). These angles correspond to the angle between earth's rotation axis and the ecliptic pole and its supplement. It follows that imposing the constraint that observations must be performed in earth's umbra will increase the cost of imaging the majority of science targets.

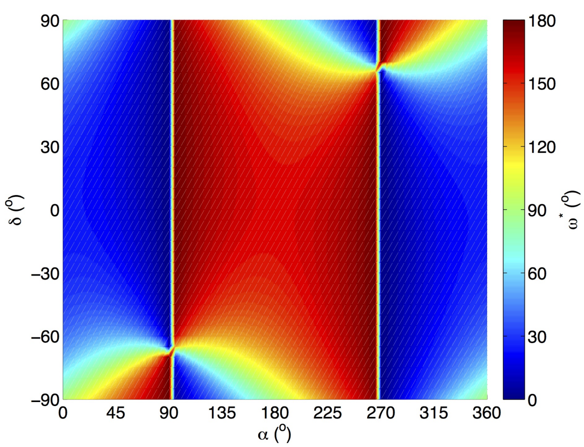

Figure 5. Plot of argument of perigee that ensures alignment of apogee with earth's umbra vs α and δ of the science target

6. High-Fidelity Simulation Description

The proposed design strategy is validated through high-fidelity numerical simulations of a reference mission profile to image various science targets including both science and reconfiguration phases. It is assumed that each mission simulation includes ten science phases, with nine corresponding reconfiguration phases. Relevant mission parameters are given in Tab. 2. The implementation of the science phase and reconfiguration phase simulations are described in the following.

Table 2. Mission simulation parameters

a (km)	e	$\bar{\rho}$ (km)	Δt (hr)
24500	0.72	500	1.5

6.1. Science Phase Simulation

The science phase simulation is conducted as follows. First, the orbit of the telescope spacecraft is specified either from the initial conditions of the mission or from the end state of a reconfiguration phase simulation. The initial orbit of the occulter spacecraft is specified by enforcing the initial condition constraints of the science phase, which include: 1) the relative position vector is aligned with the target, 2) the inertial relative velocity perpendicular to the line-of-sight is zero, and 3) the initial separation and drift rates are specified to minimize the deviation from the baseline separation (from Eq. 6). The orbits of the telescope and occulter spacecraft are propagated using a rigorous force model including contributions from static earth gravity, third body, solar radiation pressure, and atmospheric drag forces. The models used for each of these contributions are described in Tab. 3. It is assumed that the spacecraft have perfect knowledge of the relative

Table 3. High-fidelity simulation force models

Force Model Contributions	Simulation Model
Static gravity field	GGM01S (120x120) [13]
Third-body sun/moon	Analytical model [15]
Atmospheric density	Jacchia [16]
Solar radiation pressure	Cannonball, conical earth shadow

state. Accordingly, the telescope spacecraft applies a continuous thrust that precisely counteracts the differential acceleration perpendicular to line-of-sight throughout the simulation. This control force is numerically integrated to compute the total delta-v cost of the maneuver. The implementation of these simulations is illustrated in Fig. 6.

6.2. Reconfiguration Phase Simulation

To describe the impulsive reconfiguration problem, it is convenient to adopt the relative orbital elements (ROE) state representation defined by D'Amico and Montenbruck [17]. The definition of

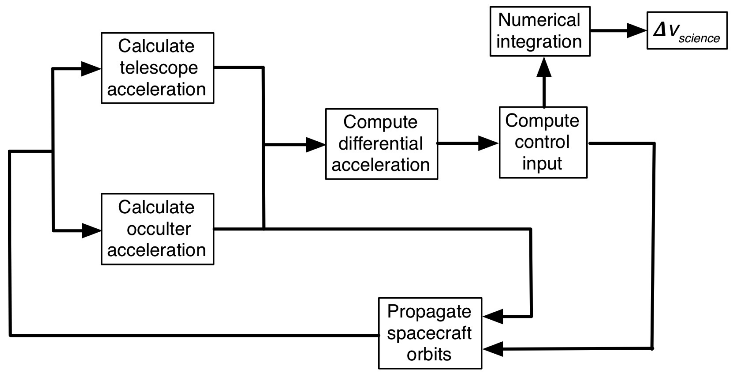

Figure 6. Science phase simulation flow chart

the ROE state is given by

$$\delta\boldsymbol{\alpha} = \begin{pmatrix} \delta a \\ \delta\lambda \\ \delta e_x \\ \delta e_y \\ \delta i_x \\ \delta i_y \end{pmatrix} = \begin{pmatrix} (a_c - a_d)/a_d \\ M_c - M_d + \omega_c - \omega_d + (\Omega_c - \Omega_d)\cos i_d \\ e_c \cos\omega_c - e_d \cos\omega_d \\ e_c \sin\omega_c - e_d \sin\omega_d \\ i_c - i_d \\ (\Omega_c - \Omega_d)\sin i_d \end{pmatrix} \tag{40}$$

where the subscripts c and d denote properties of the chief and deputy spacecraft, respectively. The reconfiguration phase simulations are based on a closed-form maneuver planning algorithm valid for orbits of arbitrary eccentricity. This algorithm uses a single cross-track impulse to correct the out-of-plane ROE (δi_x and δi_y), and a sequence of three along-track impulses to correct the in-plane ROE (δa, $\delta\lambda$, δe_x, and δe_y). This strategy nominally requires two orbits to achieve an arbitrary change in $\delta\boldsymbol{\alpha}$. For a detailed explanation of the computation of the required maneuvers, the reader is referred to Koenig et al. [8]. This maneuver planning algorithm is implemented in an iterative scheme in simulations to account for perturbations as described in the following. First, the initial state of the reconfiguration problem, $\delta\boldsymbol{\alpha}_i$, is computed by applying the osculating to mean transformation described by Schaub [18] to the relative state at the end of the science phase simulation. Next, the orbit of the telescope spacecraft is propagated using the described force model to the start of the next science phase, which is presumed to be centered at the apogee of the second orbit due to the requirements of the reconfiguration algorithm. At this point, the orbit of the occulter is specified by applying the initial condition constraints of the science phase. The desired final state of the reconfiguration problem, $\delta\boldsymbol{\alpha}_f$, is computed by applying the osculating to mean transformation to this desired state. The closed-form reconfiguration algorithm is used to compute the required impulses to take the formation from $\delta\boldsymbol{\alpha}_i$ to $\delta\boldsymbol{\alpha}_f$ and their execution times. To address the effect of perturbations, the orbit of the occulter spacecraft is propagated to the start of the next science phase including the computed maneuvers. The true end state, $\delta\boldsymbol{\alpha}_{end}$, is computed by applying the osculating to mean transformation to the relative state at the end of this propagation. Next, the maneuver sequence is recomputed with a modified end state, $\delta\boldsymbol{\alpha}_f^*$, and the propagation of the orbit of the occulter spacecraft is repeated. After each propagation, a correction is applied to the end state of the computation algorithm as given by

$$\delta \boldsymbol{\alpha}_f^* = \delta \boldsymbol{\alpha}_f^* + (\delta \boldsymbol{\alpha}_f - \delta \boldsymbol{\alpha}_{end}) \tag{41}$$

This process is iterated until $\delta \boldsymbol{\alpha}_{end}$ converges to $\delta \boldsymbol{\alpha}_f$. In practice, this iteration scheme nominally converges to sub-meter precision within five iterations. The implementation of these simulations is illustrated in Fig. 7.

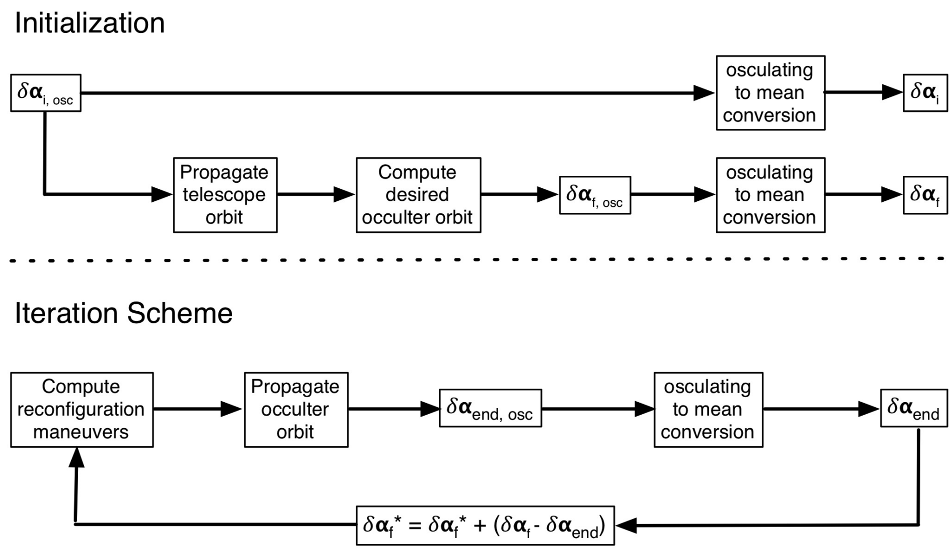

Figure 7. Reconfiguration phase simulation flow chart

7. Simulation Results

The described mission simulations are used to determine 1) the contribution of third body, solar radiation pressure, and atmospheric drag to the total cost of a mission, and 2) the effect of the location of the science target of interest on the total mission cost. The latter is studied with and without the constraint that the observations are performed with the occulter spacecraft in earth's umbra.

7.1. Third Body, Solar Radiation Pressure, and Atmospheric Drag Perturbations

The effects of third body, solar radiation pressure, and atmospheric drag forces are assessed by repeating the simulations of a reference mission to image Beta Pictoris (α = 86.75°, δ = -51.07°) described in Koenig et al. [8]. Accounting only for geopotential forces, this mission has a total delta-v cost of 2.34 m/s. This includes a 0.17 m/s cost associated with the science phases and 2.17 m/s associated with reconfiguration phases. Applying the centering procedure described above, the optimal orbit elements for the telescope spacecraft are given in Tab. 4.

Inclusion of solar radiation pressure and atmospheric drag forces requires specification of the ballistic properties of the spacecraft. According to a concurrent preliminary system design study [19],

Table 4. Initial telescope orbit specification for reference Beta Pictoris Mission

i (°)	ω_0 (°)	Ω_0 (°)	ω^* (°)	Ω^* (°)
39	88.3	357.3	90	356.75

the occulter spacecraft is presently expected to be a micro-satellite with a mass of approximately 150 kg, and a worst-case surface area of 3 m^2 with the occulter deployed. The telescope spacecraft is expected to be a 6U CubeSat with a mass of approximately 10 kg and a surface area of 0.06 m^2 on the largest side. It is assumed that both spacecraft have drag and reflectance coefficients of 2. For completeness, simulations of the reference mission were conducted allowing the mass of each spacecraft to vary by as much as a factor of 2. The differential ballistic coefficient in these simulations ranges from 20% to 90%. The total mission cost for each of these simulations did not deviate from the reference cost by more than 4%. It is therefore evident that including these perturbations has negligible impact on the delta-v cost of the reference mission. Thus, the total mission cost is driven by J_2 effects. However, it is known that third body and solar radiation pressure forces are nearly invariant with orbit radius. Thus, the costs associated with these perturbations may be significant if the formation is deployed in a larger orbit.

7.2. Cost vs Science Target Location

Because the total cost of a mission is dominated by J_2 effects, it is evident that the cost of imaging a given science target depends on its location. As shown in Eq. 31, these effects are invariant with Ω. It follows that the mission cost varies only with the declination of the the target if the earth umbra constraint is not enforced. To characterize this effect, simulations of the reference mission were conducted on a set of hypothetical science targets with declination ranging from -90° to 90°. Figure 8 (left) illustrates how the cost breakdown of these simulations varies with $|\delta|$. The total mission cost varies between 2.0 and 2.8 m/s and is dominated by the reconfiguration cost. The behavior of the cost profile suggests that the sum of the effects of absolute and differential J_2 effects cannot be simultaneously suppressed given the constraints of the formation design strategy.

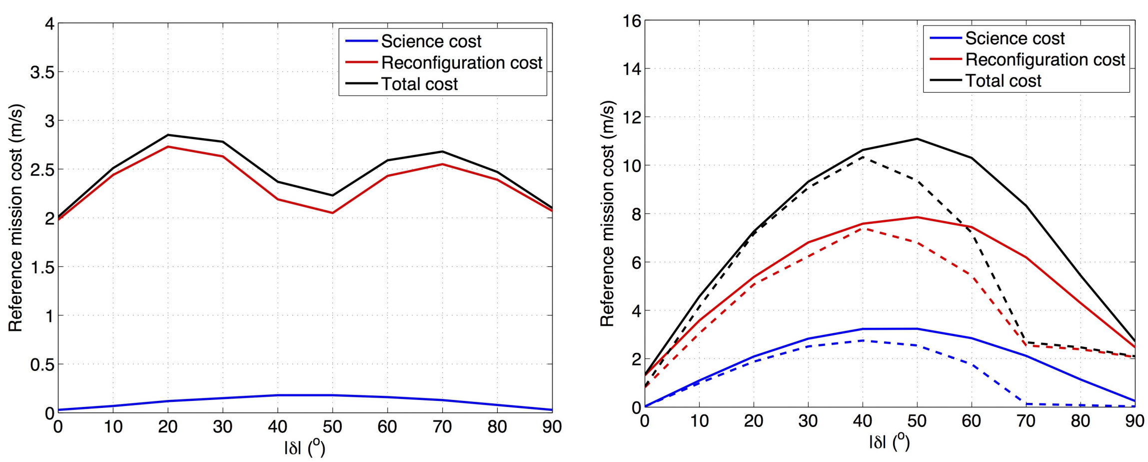

Figure 8. Reference mission cost vs δ for optimal mission configuration (left) and eclipse-constrained missions (right)

In order to characterize how the mission cost varies with target location subject to the umbra constraint, a set of simulations was conducted for a set of hypothetical targets that vary in both right ascension and declination. For each target, the initial RAAN and argument of perigee are selected to center the orbit about the configuration defined by Eq. 26 and Eq. 39. Figure 8 (right) shows how the cost breakdown of these simulations varies with $|\delta|$. The dashed lines denote the minimum cost for each declination value and the solid lines denote the maximum cost. Several conclusions can be drawn from this plot. First, the worst-case delta-v cost for imaging any target subject to the umbra constraint is 11.6 m/s, which is still well within the delta-v budget of current small satellite propulsion systems [20]. Second, the best-case delta-v cost for simulations with $|\delta|$ ranging from 10° to 70° is much larger than the cost associated with the optimal configuration. In this region the argument of perigee must be close to 23° or 157°, which causes the pointing vector to the target at the apogee to evolve in the R direction. This results in large increases in both the science and reconfiguration phase costs. Simulations with $|\delta|$ between 70° to 90° instead show a wide range of possible costs. This is because the required argument of perigee can take on any value depending on the exact location of the science target. Finally, for targets near the equator ($|\delta| \leq 5^{\circ}$) the total cost can be as low as 0.85 m/s, which is much less than the cost associated with the proposed formation design strategy for any declination. Furthermore, this minimum cost occurs when the argument of perigee is 0° or 180°. This is in direct conflict with the argument of perigee provided by the described formation design strategy. To understand this phenomenon, consider the following. First, recall that the argument of perigee was specified to ensure that the pointing vector to the target evolves in the TN-plane. It is evident from Eq. 26 that aligning the angular momentum vector with an equatorial target requires a polar orbit. Polar orbits do not exhibit secular drift of Ω, so the angular momentum vector of the orbit will be properly aligned for the expected mission lifetime regardless of the choice of ω. Additionally, it was found that formations with an argument of perigee of 0° or 180° are characterized by a near zero difference in semi-major axis, eccentricity, and inclination. It follows that these formations are not subject to differential J_2 effects. The resulting reconfiguration costs are due only to the secular drift of ω. On the other hand, formations with an argument of perigee of 90° exhibit a large difference in inclination, which causes differential J_2 effects. The cost associated with these effects is small compared with the costs associated with allowing the angular momentum vector of the orbit to drift in an unfavorable manner for all cases except polar orbits.

8. Conclusions

This paper builds upon a novel formation design strategy for a miniaturized distributed occulter/telescope in earth orbit which has been demonstrated to minimize the delta-v cost associated with both forced motion control and impulsive reconfiguration maneuvers. The design strategy is based on the idea that the delta-v cost of forced motion control is minimized by allowing the spacecraft to drift along the line-of-sight. The contribution of this paper to the state of the art is twofold. First, it was demonstrated that third body, solar radiation pressure, and atmospheric drag forces have negligible impact on the delta-v cost of nominal operations. Second, the delta-v cost of a reference mission was characterized as a function of the location of the science target with and without a constraint that observations must be performed with the occulter spacecraft in earth's umbra. These simulations demonstrated that the proposed design strategy minimizes mission costs for the vast majority of possible science targets. These simulations also demonstrated that equatorial targets allow favorable observation conditions with respect to J_2 effects. Finally, these simulations suggest that the cost of imaging an arbitrary science target is well within the delta-v budget of current small satellite propulsion systems.

The conclusions of this work call for a number of follow-on studies. First, a more detailed study of the costs associated with mission operations is warranted. Such a study would include the costs associated with the limitations of realistic guidance, navigation, and control systems (e.g. navigation and maneuver execution errors) and costs associated with other phases of mission operations such as formation acquisition. Second, in order to increase the science return of a small-scale mission, the proposed formation design strategy must be generalized to a mission to image multiple science targets.

Overall, this paper demonstrates that deployment of a miniaturized distributed occulter/telescope on micro- or nano-satellites in earth orbit to image an exozodiacal dust disk is feasible with current propulsion technology provided that the absolute and relative orbits are properly selected. Deployment of such a mission could demonstrate the validity of the distributed occulter/telescope concept and provide a valuable science return at a small fraction of the cost of large-scale platforms.

9. References

[1] Borucki, W. J., Koch, D. G., Lissauer, J. J., Basri, G. B., Caldwell, J. F., Cochran, W. D., Dunham, E. W., Geary, J. C., Latham, D. W., Gilliland, R. L., Caldwell, D. A., Jenkins, J. M., and Kondo, Y. "The Kepler mission: a wide-field-of-view photometer designed to determine the frequency of Earth-size planets around solar-like stars." "Astronomical Telescopes and Instrumentation," pp. 129–140. International Society for Optics and Photonics, 2003.

[2] D'Amico, S., Ardaens, J.-S., and Larsson, R. "Spaceborne autonomous formation-flying experiment on the PRISMA mission." Journal of Guidance, Control, and Dynamics, Vol. 35, No. 3, pp. 834–850, 2012.

[3] Landgraf, M. and Mestreau-Garreau, A. "Formation flying and mission design for Proba-3." Acta Astronautica, Vol. 82, No. 1, pp. 137–145, 2013.

[4] Roscoe, C. W. T., Vadali, S. R., Alfriend, K. T., and Desai, U. P. "Optimal formation design for magnetospheric multiscale mission using differential orbital elements." Journal of Guidance, Control, and Dynamics, Vol. 34, No. 4, pp. 1070–1080, 2011.

[5] Seager, S., Cash, W. C., Kasdin, N. J., Sparks, W. B., Turnbull, M. C., Kuchner, M. J., Roberge, A., Domagal-Goldman, S., Shaklan, S., Thomson, M., Lisman, M., Martin, S., and Webb, D. "Exo-S: A Probe-scale Space Mission to Directly Image and Spectroscopically Characterize Exoplanetary Systems Using a Starshade and Telescope System." "American Astronomical Society Meeting Abstracts," Vol. 224. 2014.

[6] Cash, W. "Detection of Earth-like planets around nearby stars using a petal-shaped occulter." Nature, Vol. 442, No. 7098, pp. 51–53, 2006.

[7] Koenig, A. W., D'Amico, S., and Macintosh, B. "A Pareto-Optimal Characterization of Small-Scale Distributed Occulter/Telescope Systems." "Optical Engineering+Applications," International Society for Optics and Photonics, 2015.

[8] Koenig, A. W., D'Amico, S., Macintosh, B., and Titus, C. J. "Optimal Formation Design of a Miniaturized Distributed Occulter/Telescope in Earth Orbit." "Proceedings of the AIAA/AAS Astrodynamics Specialist Conference," 2015.

[9] Graham, J. R., Kalas, P. G., and Matthews, B. C. "The Signature of Primordial Grain Growth in the Polarized Light of the AU Microscopii Debris Disk." The Astrophysical Journal, Vol. 654, No. 1, p. 595, 2007.

[10] Moór, A., Ábrahám, P., Derekas, A., Kiss, C. S., Kiss, L. L., Apai, D., Grady, C., and Henning, T. H. "Nearby Debris Disk Systems with High Fractional Luminosity Reconsidered." The Astrophysical Journal, Vol. 644, No. 1, p. 525, 2006.

[11] Peters, T. V., Branco, J., Escorial, D., Castellani, L. T., and Cropp, A. "Mission analysis for PROBA-3 nominal operations." Acta Astronautica, Vol. 102, pp. 296–310, 2014.

[12] Vallado, D. A. and McClain, W. D. Fundamentals of astrodynamics and applications, Vol. 12. Springer Science & Business Media, 2001.

[13] UT/CSR. "GRACE Gravity Field Model GGM01." Tech. rep., University of Texas, Center for Space Research, 2003. Http://www.csr.utexas.edu/grace/gravity/ggm01/GGM01Notes.pdf.

[14] Breger, L. and How, J. P. "Gauss's variational equation-based dynamics and control for formation flying spacecraft." Journal of Guidance, Control, and Dynamics, Vol. 30, No. 2, pp. 437–448, 2007.

[15] Montenbruck, O. and Gill, E. Satellite Orbits: Models, Methods and Applications. Springer Science & Business Media, 2012.

[16] Jacchia, L. G. "Revised static models of the thermosphere and exosphere with empirical profiles." "Res. Space Sci. Spec. Rep. 332," Smithson. Astrophys. Observ Cambridge, Mass, 1971.

[17] D'Amico, S. and Montenbruck, O. "Proximity operations of formation-flying spacecraft using an eccentricity/inclination vector separation." Journal of Guidance, Control, and Dynamics, Vol. 29, No. 3, pp. 554–563, 2006.

[18] Schaub, H. and Junkins, J. L. Analytical Mechanics of Space Systems. AIAA, 2003.

[19] Kolmas, J., Banazadeh, P., Koenig, A. W., and D'Amico, S. "Preliminary System Design of a Miniaturized Distributed Occulter/Telescope for Direct Imaging of Exozodiacal Dust and Exoplanets." "Proceedings of the 7th European CubeSat Symposium," 2015.

[20] Hruby, V. "High Isp CubeSat Propulsion." "Interplanetary Cubesat Conference," 2012.